Elevation Gradients of European Climate Change in the Regional Climate Model COSMO-CLM

S. Kotlarski[1], T. Bosshard[1], D. Lüthi[1], P. Pall[1], C. Schär[1]

[1]*Institute for Atmospheric and Climate Science, ETH Zurich, Switzerland*

Corresponding author:
Dr. Sven Kotlarski, Institute for Atmospheric and Climate Science, ETH Zurich , Universitätstrasse 16, CH-8092 Zürich, Switzerland, phone: +41 44 632 6672, fax: +41 44 632 13 11, email: sven.kotlarski@env.ethz.ch

- Electronic Supplementary Material (ESM) -

We here present supplementary material to our main article published in *Climatic Change*. The *ESM* contains supporting and additional analyses and is structured as follows:

Part A: Area-altitude distribution in sub-domains

As any direct analysis of the CCLM model output is limited to the elevation range represented by the mean grid cell orography, very high altitudes are not covered by our study. For instance, in our model setup (horizontal resolution of approx. 25km) the highest grid cell in the Alps is located at 2693 m, which is still considerably lower than the highest peak in this sub-domain (Mont Blanc at 4807 m). To provide an idea on the elevation range covered by the eight analysis domains, Figure ESM 1 shows the area-altitude distribution for each sub-domain based on the CCLM grid cell orography. See Figure 1 of the main article for the location of the individual sub-domains.
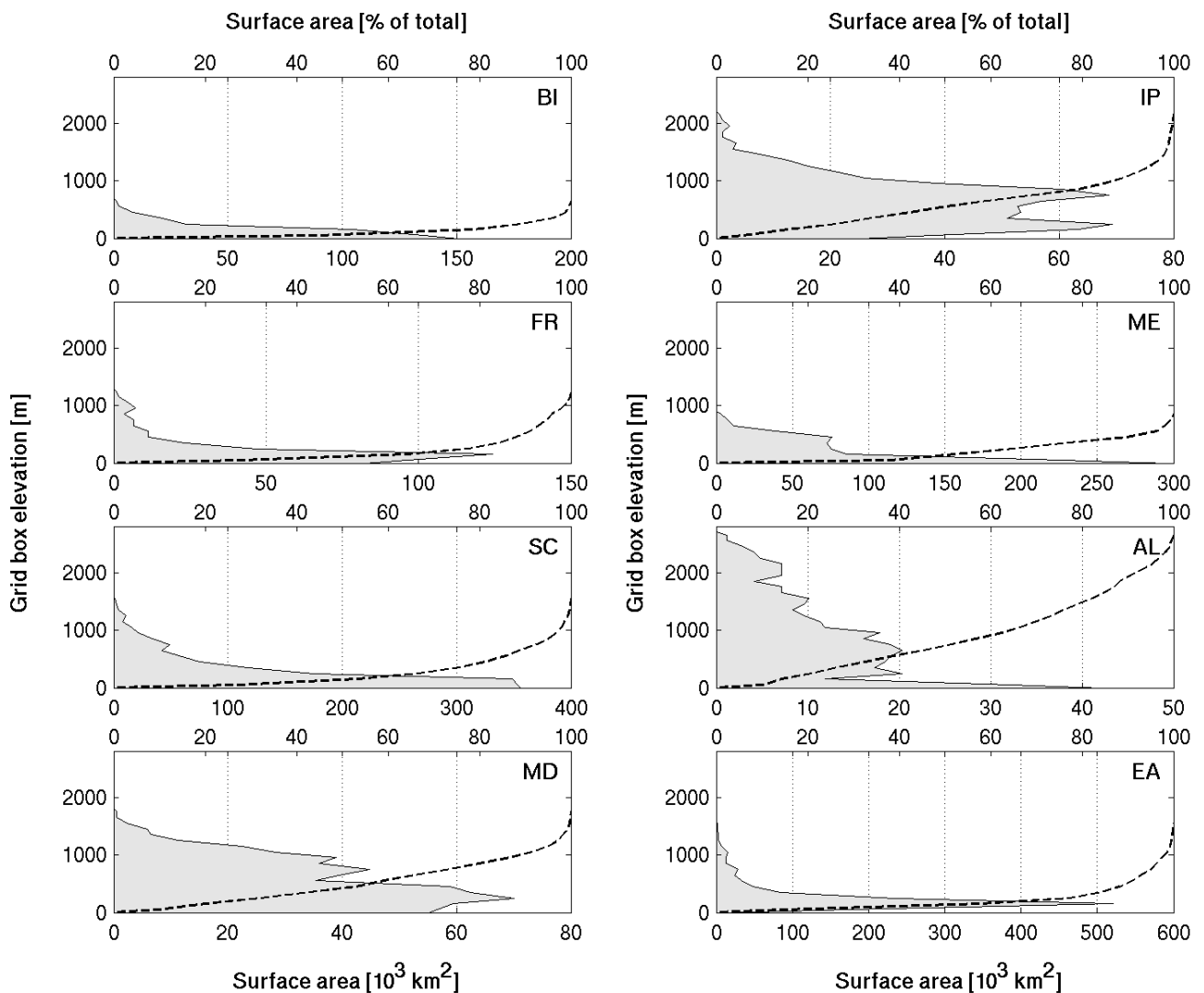

Fig. ESM 1 Area-altitude distribution of the CCLM model orography for the eight sub-domains analyzed (only land grid points). The solid line indicates the area of each 100 m elevation bin (bottom scale), the dashed line the cumulative area fraction (top scale). Note that the ordinate (altitude) is identical for all sub-domains while the abscissa (surface area) differs from panel to panel.

Part B: Evaluation of monthly temperature and precipitation elevation gradients

We here present the validation of the annual cycles of the 2m temperature lapse rate and the precipitation elevation gradient against the E-OBS reference dataset. Despite a general overestimation of the mean lapse rate, CCLM is able to approximately reproduce the annual cycle of the temperature-elevation relationship in all sub-domains (Fig. ESM 2). Depending on the region, maximum values of the lapse rate are found in winter (IP, FR, ME, MD) or in summer (BI, SC, AL, EA). In all cases, CCLM approximately captures the timing of the maxima / minima as well as the intra-seasonal variability. The largest differences between the ERA40-driven and the HadCM3-driven CCLM

experiment occur during summer, while differences during other seasons are small. For precipitation similar conclusions apply (Fig. ESM 3). The annual cycle of the precipitation-elevation relationship as well as the general magnitude of the elevation gradient are reproduced in all regions except the British Isles (BI). Here, the pronounced increase of winter precipitation with elevation as given by E-OBS is not captured by the model. Again, the differences between both model experiments are small. Note that a linear fit only provides a very rough estimate of the precipitation-altitude relation.
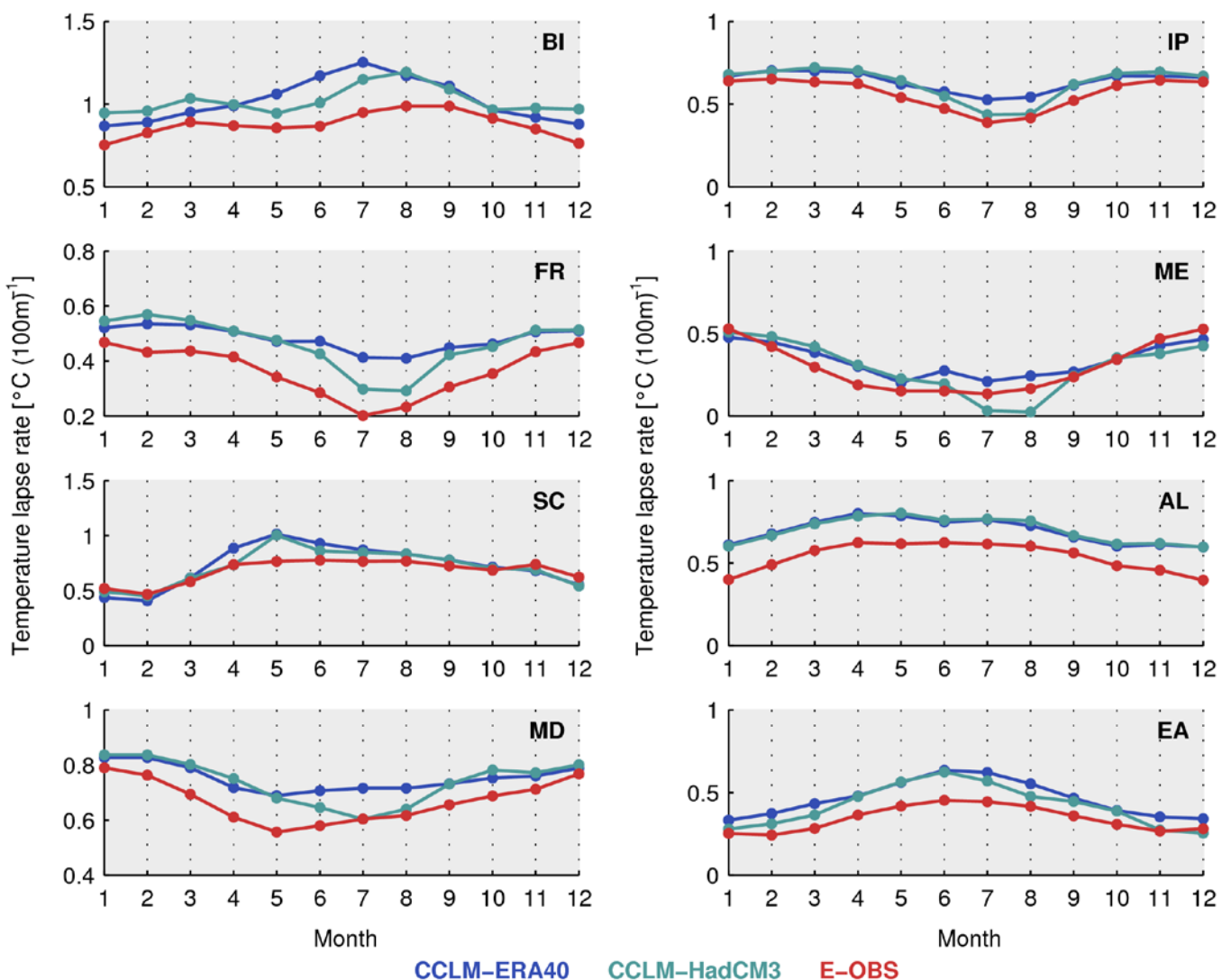

CCLM–ERA40   CCLM–HadCM3   E–OBS

Fig. ESM 2 Mean monthly near-surface temperature lapse rate [°C (100 m)$^{-1}$] for the period 1961-2000 in CCLM-ERA40 (blue), CCLM-HadCM3 (green) and E-OBS (red) for the eight sub-domains analyzed.

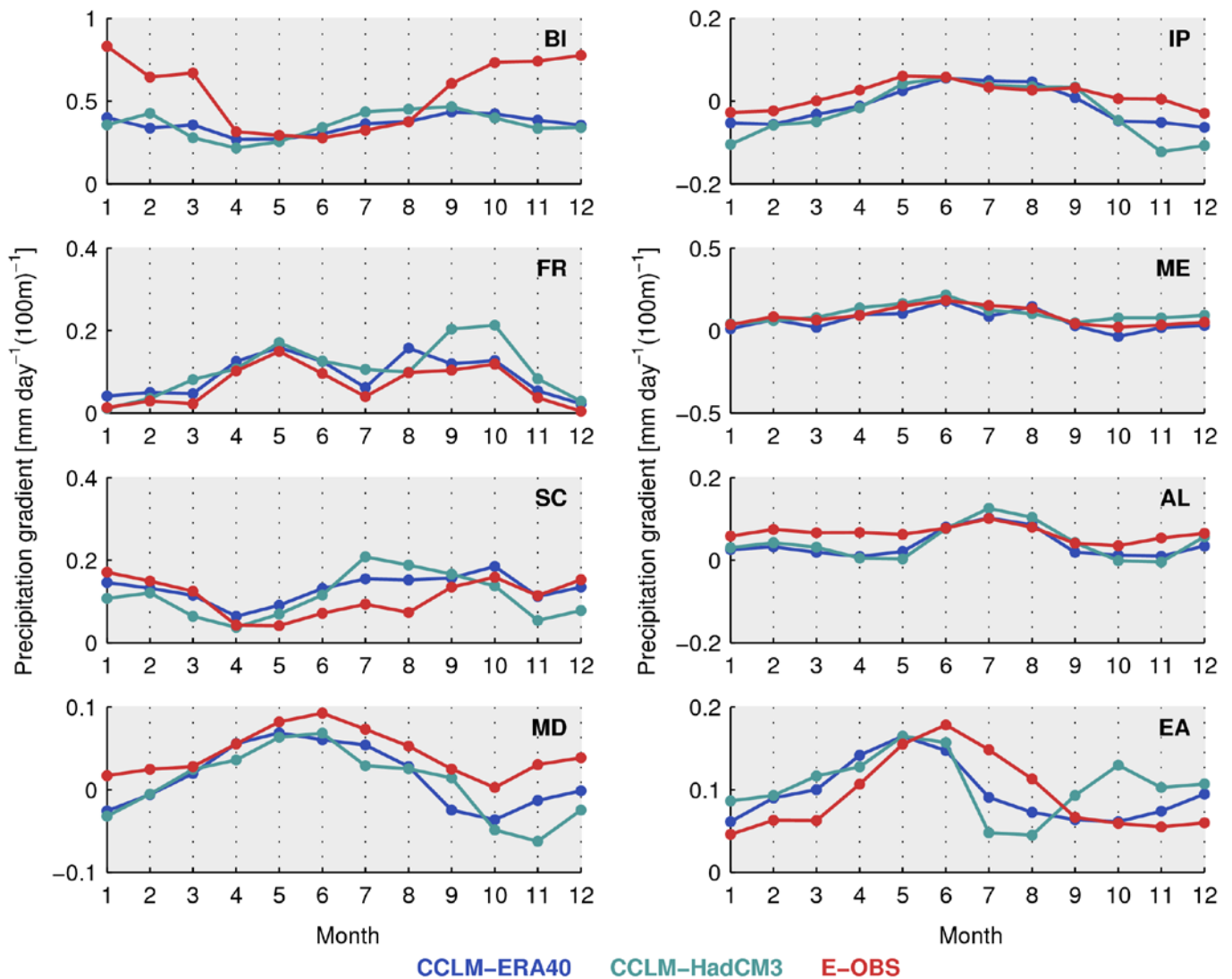**Fig. ESM 3** As Figure ESM 2 but for the mean monthly precipitation gradient [mm day^{-1} (100 m)$^{-1}$].

Part C: Evaluation of the interannual variability of the elevation dependency

Assessing CCLM's ability to represent the observed year-to-year variability of temperature and elevation dependencies is helpful for interpreting the climate change scenario. If the model's response to climate variability in the observed period corresponds to observations it would give further confidence in its potential to realistically represent the response to climate change. We here compare the linear elevation gradients of mean annual temperature and precipitation in the period 1961-2000 in CCLM-ERA40 against those derived from E-OBS.

For temperature, the interannual variability of the lapse rate is approximately represented, despite a general overestimation of the lapse rate (Fig. ESM 4). Except for sub-domain AL, temporal correlation coefficients larger than 0.5 are obtained. Also for precipitation, the model results approximately agree with E-OBS (Fig. ESM 5). Temporal correlation coefficients range from 0.26 (sub-domain ME) to 0.89 (sub-domain SC). Note, however, that a linear fit only provides a very rough estimate of the precipitation-altitude relation (see Fig. 3 of the main article).
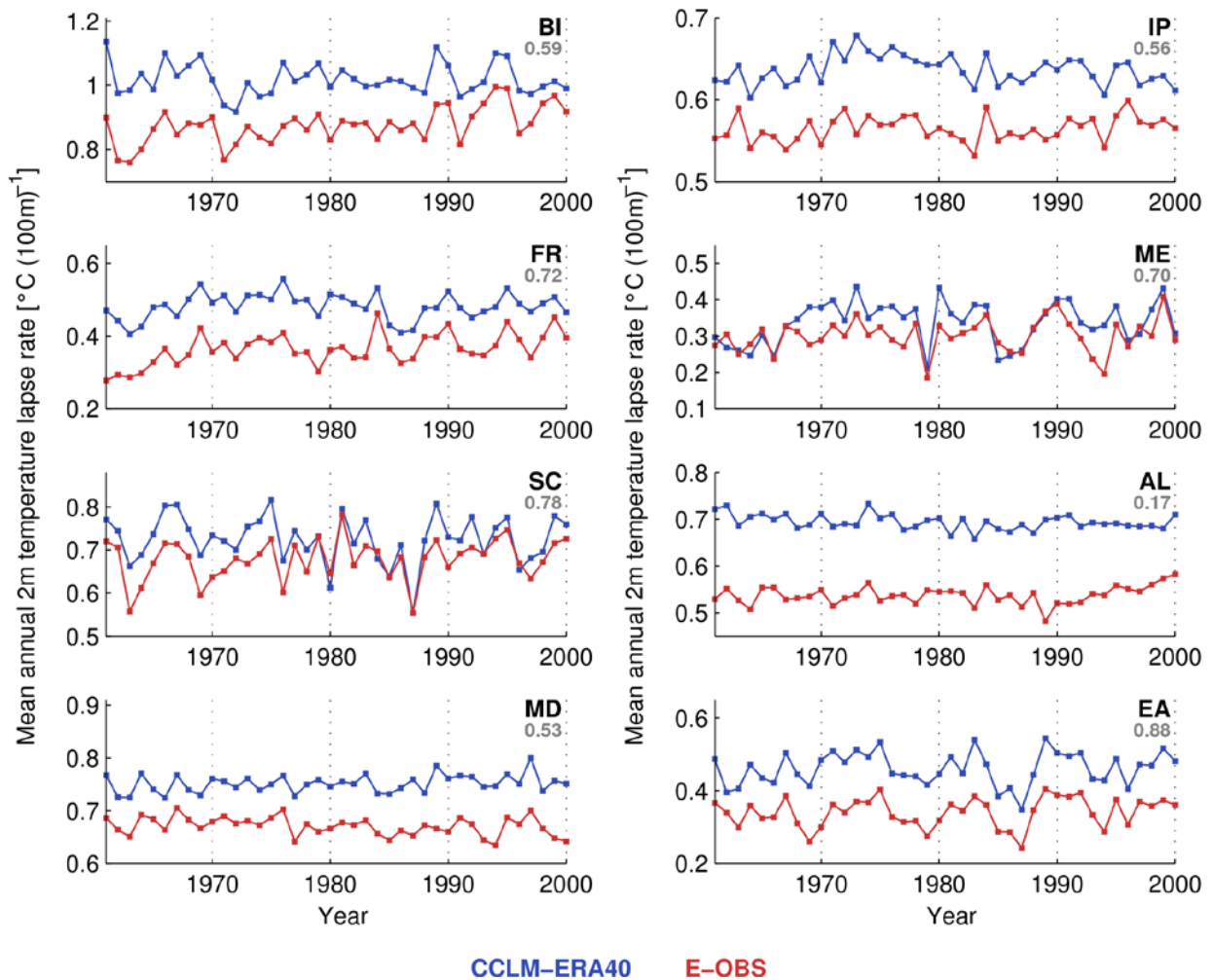
Fig. ESM 4 Mean annual temperature lapse rate [°C (100 m)$^{-1}$] in CCLM-ERA40 and E-OBS for each year in the period 1961-2000 and for each sub-domain. The gray number in the upper right corner of each panel indicates the temporal correlation coefficient.

Part D: Seasonal temperature and precipitation changes in the driving GCM HadCM3

Figures ESM 5 and ESM 6 present the mean summer and mean winter 2m temperature and precipitation changes in the GCM HadCM3, which provided the lateral boundary forcing for CCLM-HadCM3. These patterns can be compared against those of CCLM-HadCM3 (Figures 4 and 6 of the main article). Qualitatively, the seasonal change patterns as simulated by the RCM and the driving GCM agree with each other, but pronounced differences exist on a regional scale.
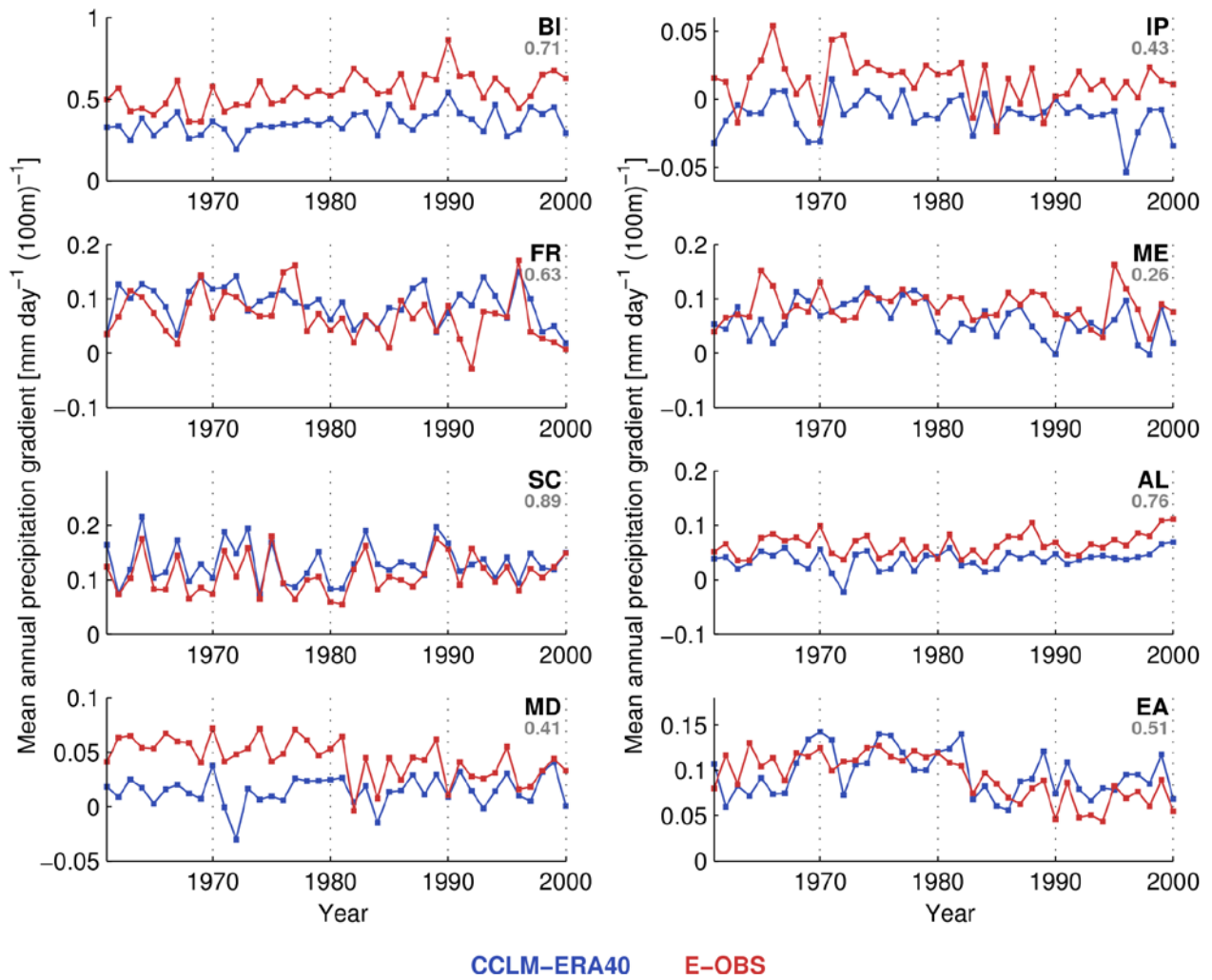
Fig. ESM 5 As Figure ESM 4 but for the linear gradient of mean annual precipitation [mm day $^{-1}$ (100 m)$^{-1}$].
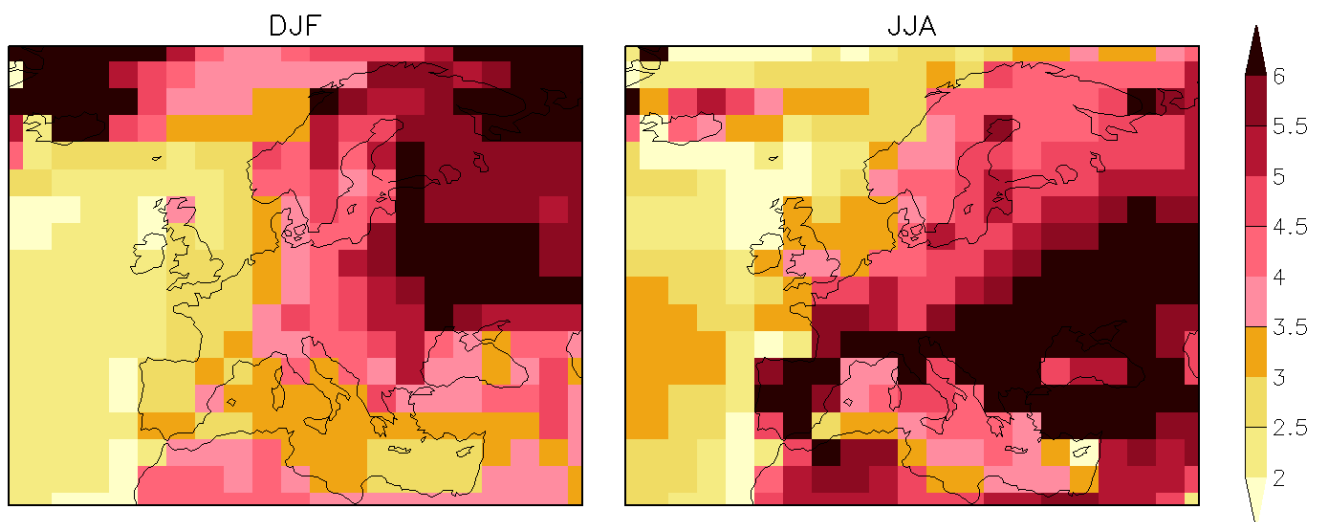

Fig. ESM 6 Simulated change of mean winter (DJF, left) and summer (JJA, right) 2m temperature between 1961-1990 and 2070-2099 in the driving GCM HadCM3 [°C].
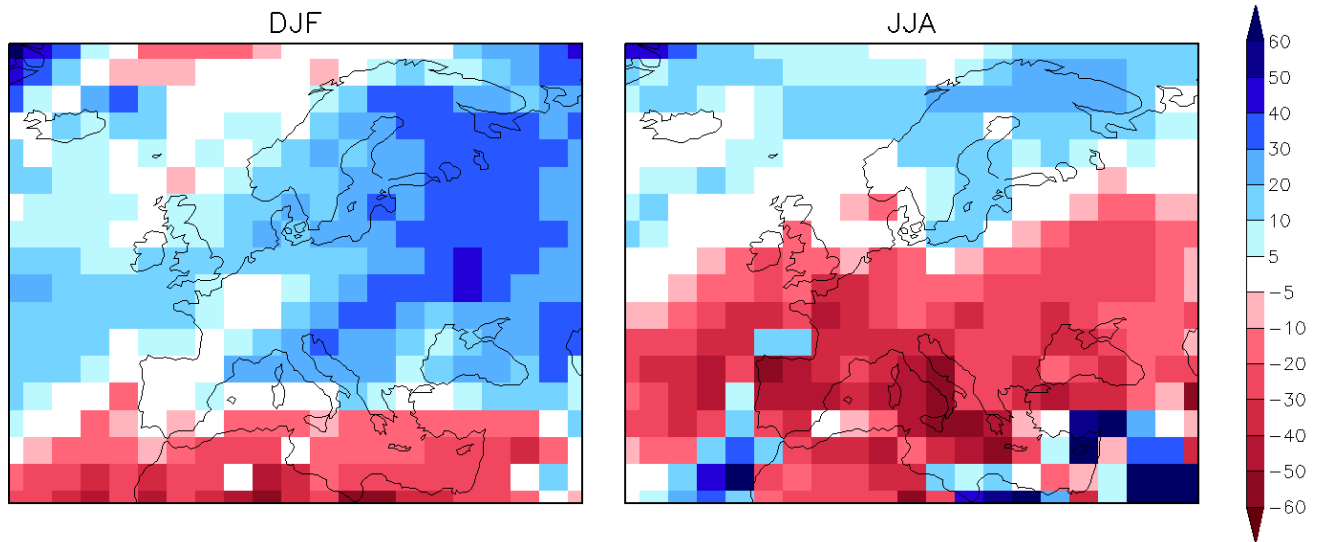
Fig. ESM 7 As Figure ESM 6 but for precipitation changes [%].

Part E: Changes of temperature lapse rates

The elevation-dependent temperature changes in CCLM-HadCM3 as described in the main article will alter surface lapse rates. A summary of mean seasonal lapse rates in the control and the scenario period, obtained by linear regression in each individual sub-domain, is given in Table ESM 1. The general pattern of larger warming rates at high elevations results in a decrease of the near-surface temperature lapse rate in most sub-domains and in most seasons (less pronounced temperature de-

crease with elevation). Typically, this effect is largest in summer with lapse rates decreasing by more than 0.1 °C (100 m)$^{-1}$ in sub-domains IP, FR and ME. Exceptions are those regions and seasons where the warming becomes less pronounced with elevation, resulting in an increase of the lapse rate, that is a stronger temperature decrease with elevation. Maximum lapse rate increases occur in sub-domain SC in winter (+0.09 °C (100 m)$^{-1}$) and in sub-domain BI in summer (+0.11 °C (100 m)$^{-1}$).

Table ESM 1 Seasonal 2m temperature lapse rate [°C (100 m)$^{-1}$] in CCLM-HadCM3 in the control period 1961-1990 (upper number) and in the scenario period 2070-2099 (lower number) for the eight sub-domains analyzed and based on linear regression. The temperature lapse rate is defined as the decrease of 2m temperature with elevation. Bold face indicates an increase of the lapse rate, i.e. a more pronounced temperature decrease with elevation.

Season		BI	IP	FR	ME	SC	AL	MD	EA
DJF	1961-1990	0.96	0.68	0.54	0.46	**0.50**	0.62	0.83	**0.28**
	2070-2099	0.95	0.65	0.50	0.46	**0.59**	0.60	0.79	**0.32**
MAM	1961-1990	0.99	0.69	0.51	0.34	**0.78**	0.77	0.75	0.47
	2070-2099	0.96	0.64	0.47	0.28	**0.80**	0.72	0.72	0.47
JJA	1961-1990	**1.11**	0.48	0.34	0.09	0.84	**0.76**	0.63	0.56
	2070-2099	**1.22**	0.37	0.24	-0.04	0.82	**0.77**	0.58	0.49
SON	1961-1990	1.02	0.67	0.46	0.31	0.73	0.63	0.76	0.36
	2070-2099	1.02	0.62	0.43	0.29	0.70	0.62	0.75	0.36

Part F: Changes of further parameters

To support our analysis in the main article, we here provide the elevation dependency of the seasonal climate change signal in CCLM-HadCM3 in the eight sub-domains for additional parameters. Figures ESM 8 and ESM 9 present the results for cloud cover and incoming solar radiation, respectively. See Chapter 3.4.3 of the main article for a discussion.
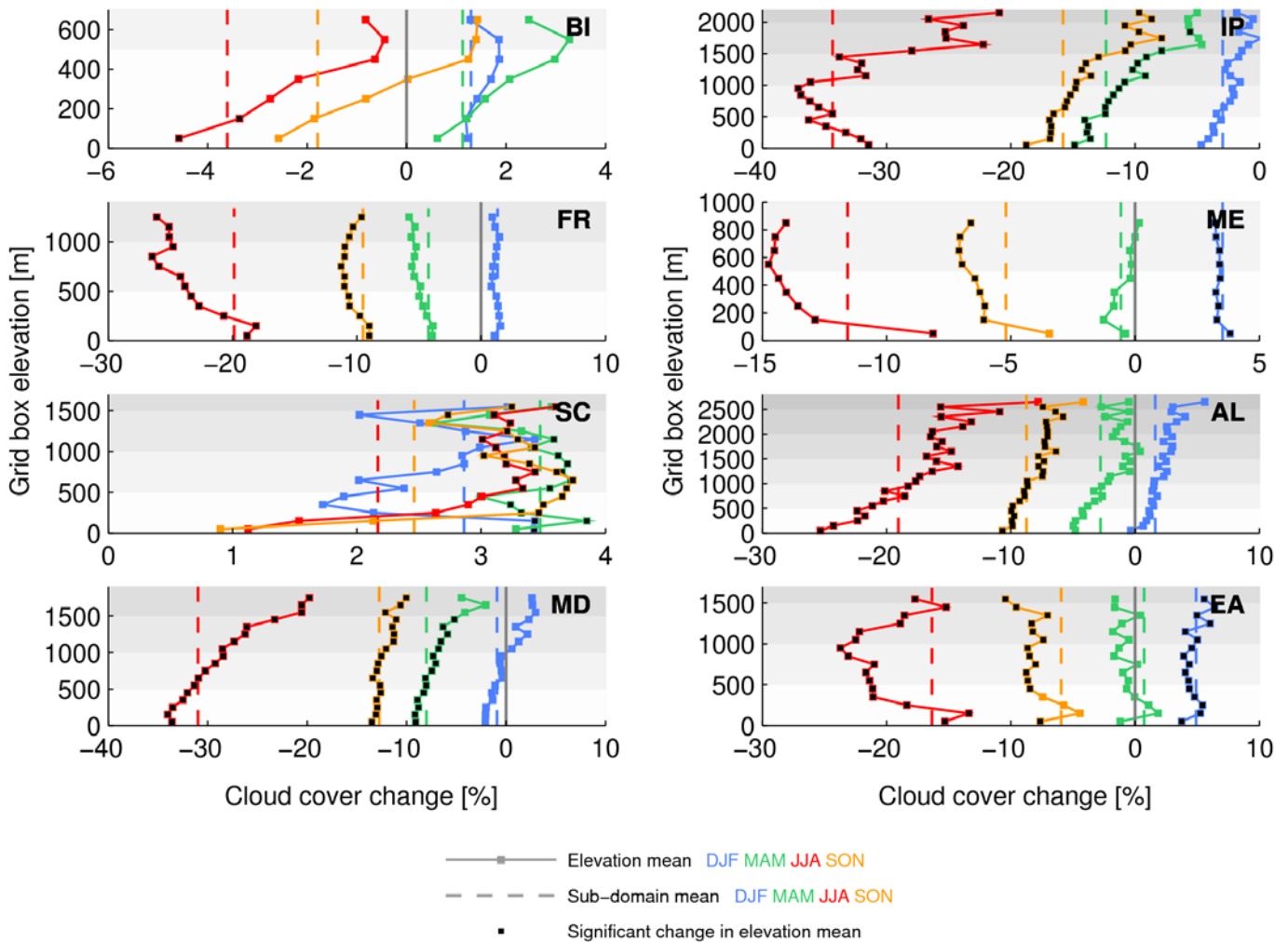

Fig. ESM 8 Simulated change of mean seasonal cloud cover between 1961-1990 and 2070-2099 [%] in each 100 m elevation interval for all seasons and all sub-domains. Black squares indicate a significant change in the respective elevation interval. The gray background shading indicates 500 m elevation bands. The same shading is used for all sub-domains to allow for a better inter-comparison.
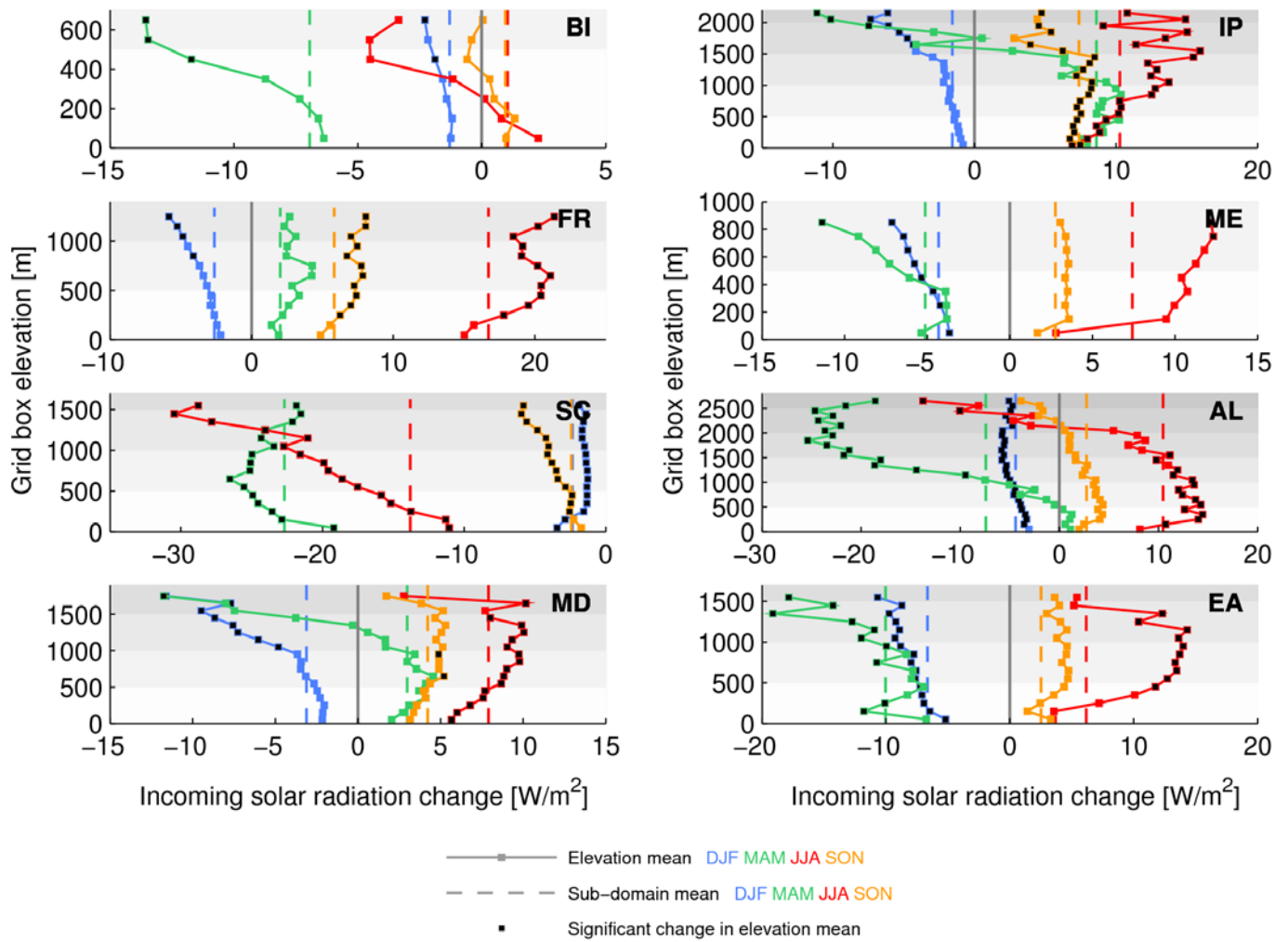
Fig. ESM 9 As Figure ESM 8 but for changes of incoming solar radiation [W/m^2].

Part G: Removing large-scale components of climate change

The sub-domain-based analysis of elevation dependencies of the climate change signal presented in the main article does not exclusively reveal pure elevation signals but can include imprints of large-scale horizontal variability. Imagine a sub-domain that shows a stronger warming in the South than in the North due to a large North-South extension and a general North-South gradient of the continental-scale warming pattern (driven by large-scale processes). If high-elevation regions within that sub-domain are exclusively located in the South, the warming will be stronger at high elevations only as a consequence of the continental-scale warming pattern and even in the absence of regional processes that are driven by the topographic height of a grid cell. Hence, large-scale warming patterns have a potential to mask "true" elevation dependencies of the climate change signal (i.e., elevation dependencies that are indeed governed by the topographic height).

In order to separate the contribution of regional-scale processes and continental-scale patterns we employ a heuristic method to reduce the influence of large-scale components onto the near-surface climate change signal. In the case

of temperature, we derive a large-scale component ΔT^{ls} of the seasonal climate change signal at each grid cell by applying a 45x45 grid box filter to the spatial pattern of the actually simulated seasonal temperature changes ΔT at the individual grid cells:

$$\Delta T^{ls}(x,y) = \frac{1}{n} \sum_{i=x-22}^{j=x+22} \sum_{j=y-22}^{j=y+22} \Delta T(i,j)$$

where x and y denote the grid box index in x- and y-direction and n the number of land grid cells available for averaging in a +/- 22 grid cell range ($n \le 2025$). Sea grid cells are not considered. The resulting spatial pattern of the seasonal ΔT^{ls} is strongly smoothed compared to that of ΔT (see Figure ESM 10 and compare it to Figure 4 of the main article). It represents large-scale variations of the temperature

change and contains only little regional variability (note that variabilities on a regional scale cannot be expected to be completely removed). Subtracting ΔT^{ls} from ΔT only leaves that component ΔT^{*} of the total temperature change which is generated by regional processes and, hence, possibly influenced by the regional topographic setting:

$$\Delta T^{*}(x,y) = \Delta T(x,y) - \Delta T^{ls}(x,y)$$

The analysis of elevation dependencies of the climate change signal is then repeated, but now using the regional component ΔT^{*} instead of the total 2m temperature change ΔT (see Section 3.7 of the main manuscript). For precipitation, the same method is applied (compare Figure ESM 11 to Figure 6 of the main article).
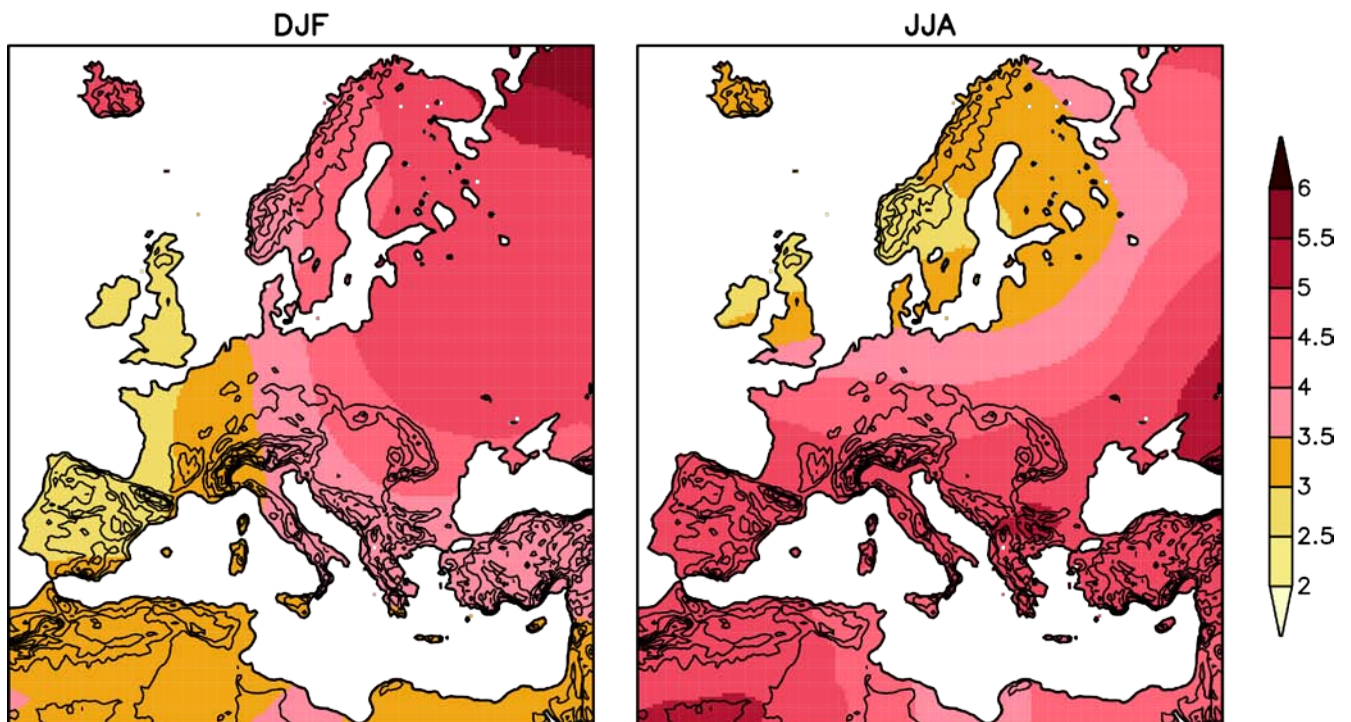

Fig. ESM 10 Simulated change of mean winter (DJF, left) and summer (JJA, right) 2m temperature between 1961-1990 and 2070-2099 [°C] . The contour lines represent the model topography at 400 m intervals. The spatial pattern of the climate change signal was smoothed by applying a 45x45 grid box filter only taking into account land grid cells.
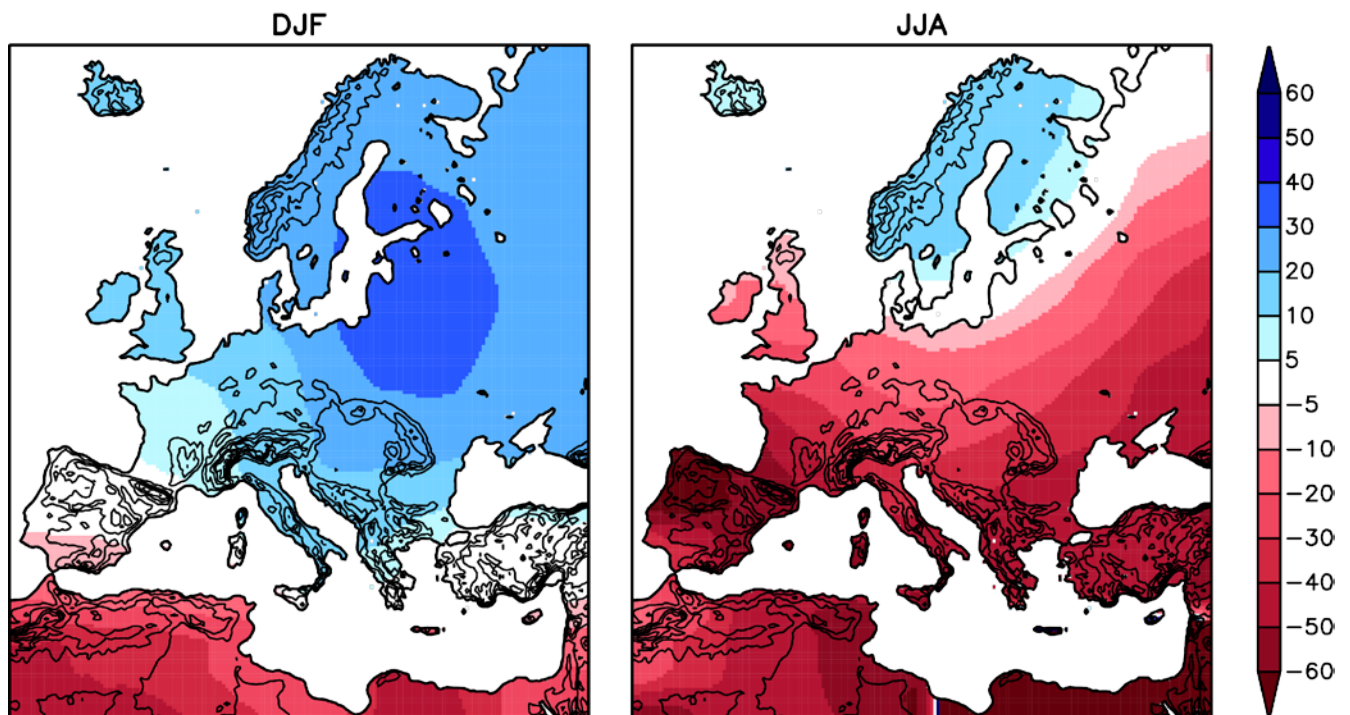
Fig. ESM 11 As Figure ESM 10 but for mean seasonal precipitation [%].

Part H: Snow cover evaluation

In the main article, snow cover is identified as an important parameter that potentially generates feedbacks onto the climate change signal. Hence, an accurate representation of contemporary snow cover characteristics in CCLM would increase our confidence into the simulated climate change pattern. A detailed snow cover evaluation is, however, beyond the scope of the current study. Nevertheless, we here present a basic evaluation to show that CCLM is indeed able to approximately capture the onset and the meltout of snow cover on a European scale. For this, we compare (a) the average total number of snow-covered weeks (b) the average first snow-covered week in the year and (c) the average last snow-covered week in the year in both CCLM-ERA40 and CCLM-HadCM3 against the *NSIDC Northern Hemisphere EASE-Grid Weekly Snow Cover*

and Sea Ice Extent Version 3[1] (averages for the period 1967-2000). The latter is a combined snow cover and sea ice extent dataset derived from satellite observations. It is provided on a 25 km equal-area grid, i.e. at a horizontal resolution comparable to the one of CCLM. The source grid resolution, however, is much coarser and varies between approx. 125 and 200 km. Snow cover data is available up from October 1966. For the comparison against the weekly NSIDC dataset, the modeled daily snow cover on grid cell level is aggregated to a weekly resolution by counting the number of snow-covered days per week and by assuming

---

[1] Armstrong, R. L., and M. J. Brodzik. 2005, updated 2007. *Northern Hemisphere EASE-Grid Weekly Snow Cover and Sea Ice Extent Version 3*. Boulder, Colorado USA: National Snow and Ice Data Center (NSIDC). Digital media. Available from *http://nsidc.org/data/nsidc-0046.html*

a snow-covered week if four or more days have snow cover. A snow-covered day, in turn, is defined as a day with a mean snow depth of at least 0.003 m w.e. (consistent with the threshold used for the analyses in the main article). As can be seen from Figure ESM 12, CCLM approximately captures the spatial variability of the length, the onset and the end of the snow-covered season throughout Europe. This provides confidence in an accurate representation also of future snow cover changes and of their feedbacks onto the temperature climate change signal.
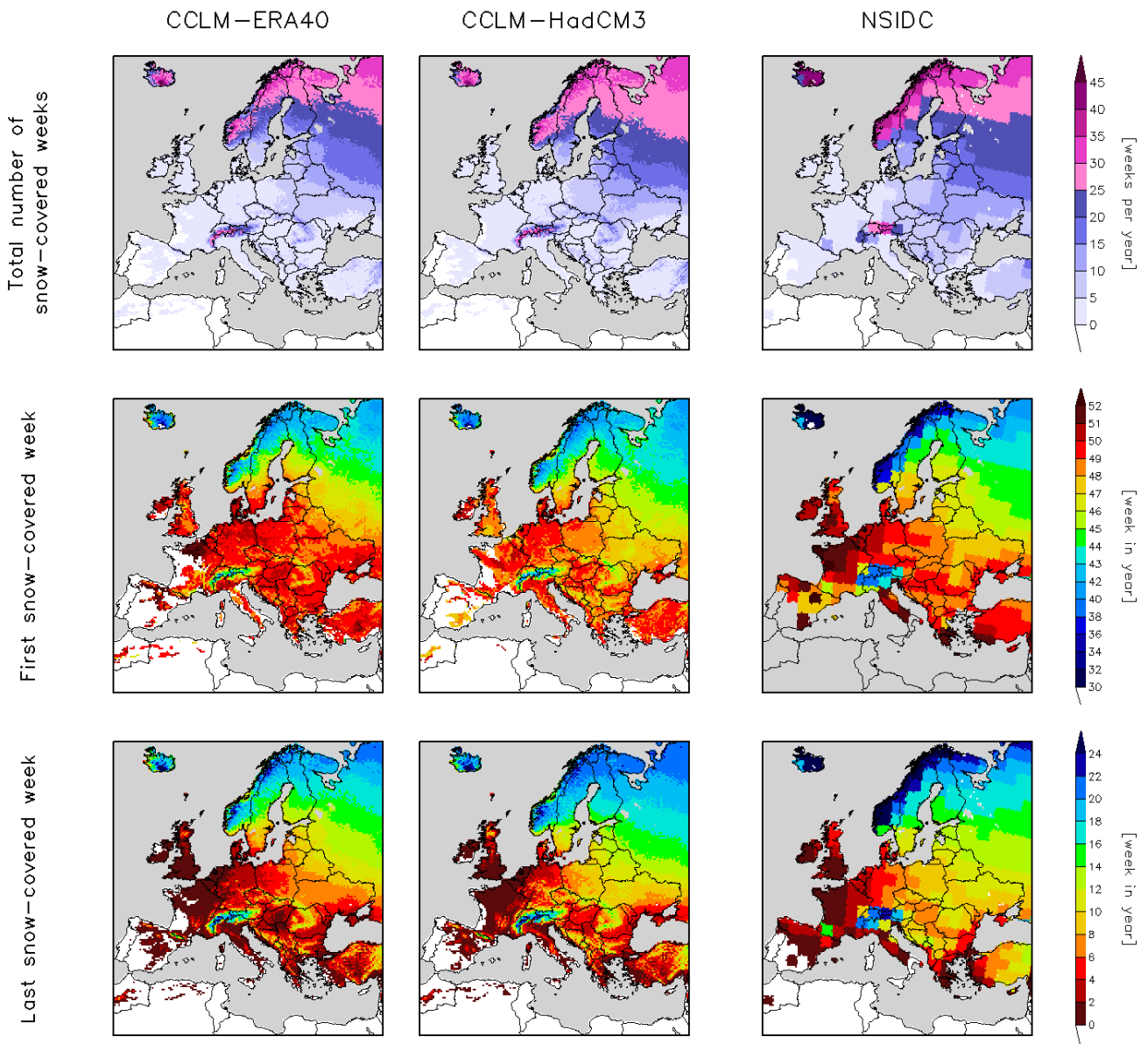

Fig. ESM 12 Comparison of different snow cover parameters in CCLM-ERA40 (left) and CCLM-HadCM3 (middle) against the NSIDC observational dataset (right) as averages over the period 1967-2000. Upper row: Total number of snow-covered weeks per year. Middle row: First snow-covered week in the year. Bottom row: last snow-covered week in year.

Part I: Influence of sea surfaces on the temperature change signal

As can be seen from Figure 4 of the main article, sea surfaces typically experience at less pronounced warming compared to land areas. This is especially true during the summer season. The low warming over sea grid cells, in turn, can be expected to influence the warming at adjacent low-elevation land grid cells. We carried out an additional analysis in order to illustrate the relation between the temperature change signal over land and the distance to the sea. We first derived the distance of each land grid cell from the sea in terms of number of grid cells (i.e., a land grid cell located at the coast line would have a distance of *1*). For each land grid cell, we then computed the difference between the mean seasonal temperature change at this grid cell and the (mean) temperature change at the closest sea grid cell(s). Finally, for each sub-domain the temperature differences where averaged for all land grid cells with a given distance to the sea. For most regions and most seasons, the difference between land surface and sea surface warming rates increases when moving landwards (Fig. ESM 13). Coastal grid cells (distance = *1*) typically show the smallest warming difference compared to their sea surface counterpart. Exceptions are BI, SC and AL. For IP, FR, ME, MD and EA especially the summer warming can strongly depend on the distance from the sea. As high-elevation areas in these regions are often found in the interior part, the land-sea effect can be excepted to contribute to the anomalous high-elevation summer warming. Please note that Figure ESM 5 does not reveal the land-sea effect alone, but a combination of all factors including the elevation effect.
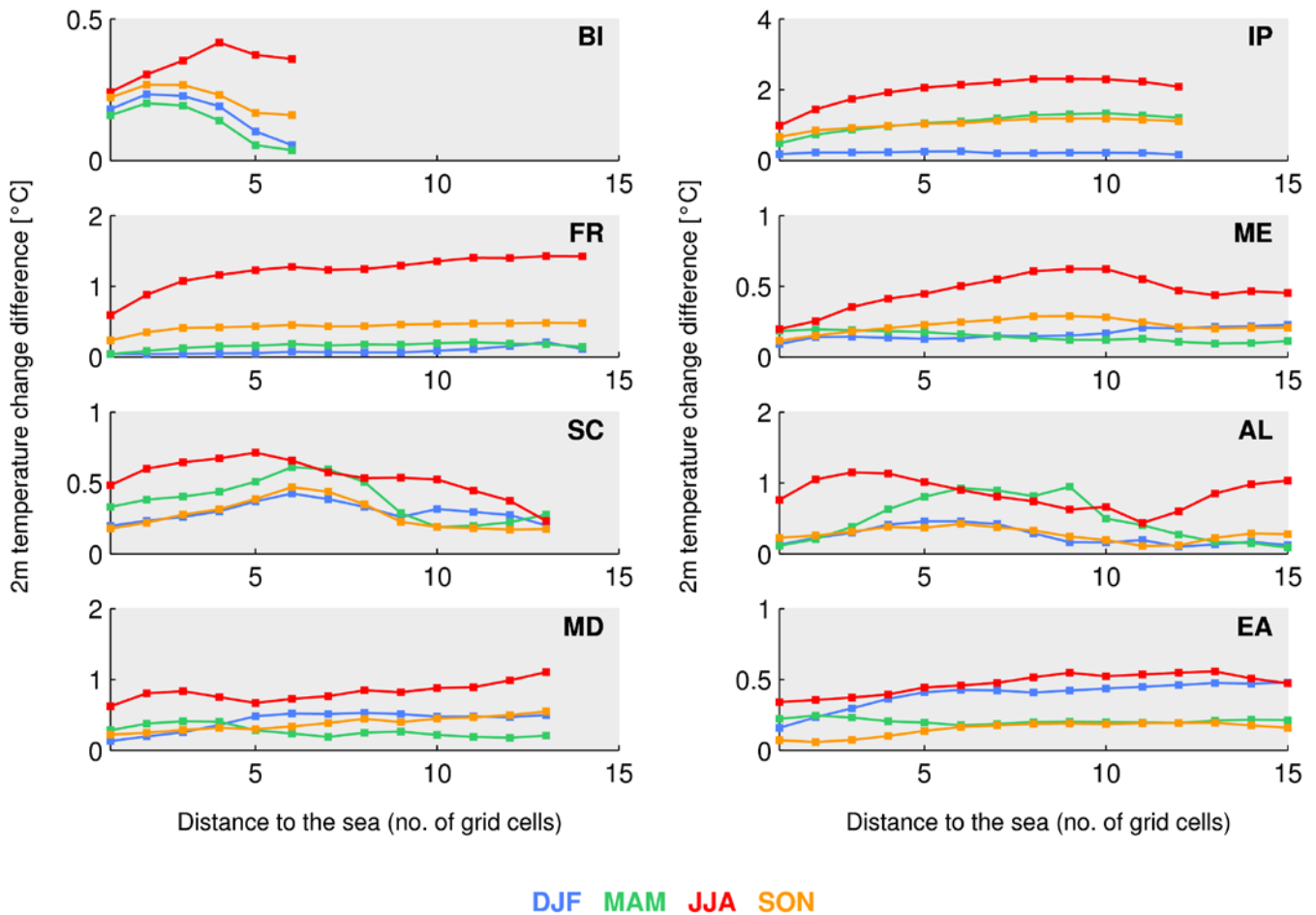

Fig. ESM 13 Mean absolute difference between the seasonal temperature change over land (1961-1990 to 2070-2099) and the temperature change at the closest sea grid cell [°C], averaged over all grid cells with a certain distance to the sea in the respective sub-domain. Only distances up to 15 grid cells are shown.